A robust estimate of continental-scale terrestrial carbon sinks using GOSAT XCO_2 retrievals

Lingyu Zhang[1], Fei Jiang[1,2,7*], Wei He[1], Mousong Wu[1], Jun Wang[1], Weimin Ju[1,2,7], Hengmao Wang[1], Yongguang Zhang[1,2,7], Stephen Sitch[3], Anthony P. Walker[4], Xu Yue[5], Shuzhuang Feng[1], Mengwei Jia[1], Jing M. Chen[6]

[1]Jiangsu Provincial Key Laboratory of Geographic Information Science and Technology, International Institute for Earth System Science, Nanjing University, Nanjing, 210023, China.

[2]Jiangsu Center for Collaborative Innovation in Geographical Information Resource Development and Application, Nanjing, 210023, China.

[3]College of Life and Environmental Sciences, University of Exeter, Exeter, UK.

[4]Environmental Sciences Division and Climate Change Science Institute, Oak Ridge National Laboratory, Oak Ridge, TN, USA,

[5]School of Environmental Science and Engineering, Nanjing University of Information Science & Technology (NUIST), Nanjing, China,

[6]Department of Geography and Planning, University of Toronto, Toronto, Ontario M5S3G3, Canada.

[7]Frontiers Science Center for Critical Earth Material Cycling, Nanjing University, Nanjing, 210023, China.

*Corresponding author: Fei Jiang (jiangf@nju.edu.cn)

Key Points:

- Terrestrial carbon sinks estimated based on GOSAT XCO_2 and 12 net ecosystem exchanges using atmospheric inversion method.
- The uncertainty reduction rates decrease significantly at decreasing spatial scales.
- The GOSAT XCO_2 can only promise a robust continental-scale net ecosystem exchange estimate.

Abstract

Satellite XCO_2 retrievals could improve the estimates of surface carbon fluxes, but it remains unknow on what scales these estimates are robust. Here, we use the time-dependent Bayesian synthesis top-down method and prior net ecosystem exchanges (NEEs) from 12 terrestrial biosphere models (TBMs) to infer the monthly carbon fluxes of 51 land regions with constraints by GOSAT XCO_2 retrievals. We find that the uncertainty (standard deviation of 12 TBMs) reduction rates (URR) decrease significantly at decreasing spatial scales. On the continental-scale, the mean URR is about 60%, and the annual and seasonal cycle estimates of NEE are rather robust. The evaluation shows that the posterior CO_2 concentrations are significantly improved at the continental scale. Our study suggests that the GOSAT XCO_2 can only promise a robust continental-scale NEE estimate, and improving the XCO_2 accuracy is an effective way to achieve robust estimates on smaller scales under current spatial coverage.

Plain Language Summary

Satellite-based CO_2 measurement can improve the estimates of surface carbon fluxes due to its relatively well global coverage, but it remains unknow on what spatial scales that the satellite observation could provide a robust estimate. Here, net ecosystem exchanges (NEEs) from 12 terrestrial biosphere models (TBMs) of 51 land regions for the period of 2011-2014 are constrained using GOSAT XCO_2 retrievals, and the uncertainty (standard deviation of 12 TBMs) reduction rates (URR) at different spatial scales are analyzed. We find that 1) from the whole globe to the mean of 51 regions, the URR decreases from 85% to 19%. 2) On the continental-scale, the mean URR is about 60%, and the annual NEEs in Asia, N. America, Europe, S. America, Africa, and Australia are estimated to be -2.15±0.23, -0.96±0.07, -0.60±0.20, -0.55±0.25, -0.49±0.14, and -0.06±0.1 PgC yr^{-1}, respectively. Our study suggests that the GOSAT XCO_2 can only promise a robust continental-scale NEE estimate, and improving the XCO_2 accuracy is an effective way to achieve robust estimates on smaller scales under current satellite observing capacity.

1 Introduction

Terrestrial ecosystems and oceans absorb about half of anthropogenic carbon emissions(Friedlingstein et al., 2020), slowing down the increase of CO_2 in the atmosphere and thus mitigates climate change. Accurate estimation of terrestrial carbon sinks and sources is an indispensable step to understand the status and the potential of their roles in regulating climate change. As a major way of constraining terrestrial carbon flux estimates with observations over large scales, top-down atmospheric inversion infers carbon fluxes from atmospheric CO_2 mole fraction observations and a priori flux, which can effectively reduce the uncertainty of carbon flux estimates(Thompson et al., 2016). At the global or hemisphere scale, the carbon flux estimates from various atmospheric CO_2 inversions are in a relatively good agreement, but at continental or regional scales, the agreement is greatly weakened due to errors in either inversion methods or observational data(Baker et al., 2006; Deng & Chen, 2011).

In situ CO_2 observations have been widely used in past atmospheric CO_2 inversions (Baker et al., 2006; Deng & Chen, 2011; Gurney et al., 2002; Jiang et al., 2013; Monteil et al., 2020; Peylin et al., 2013). Due to the uneven distribution of global surface CO_2 observations, relatively consistent results can be obtained in places where observations are densely distributed, e.g., Europe and North America (N. America). However, inversion results have high uncertainty

in areas with sparse distributions of observations(Maksyutov et al., 2013). The uneven distribution of observations leads to greatly differences in the capability of inversions to constrain the land carbon cycle in different regions(Gurney et al., 2002). Satellite-based CO_2 measurements provide global coverage with high spatial resolutions(Baker et al., 2010). Many studies have estimated regional carbon sources and sinks using column averaged dry air mole fractions of CO_2 (XCO_2) from GOSAT and OCO-2 satellites(Baker et al., 2010; Basu et al., 2013; Chevallier et al., 2014; Crowell et al., 2019; Deng et al., 2014; Jiang et al., 2021; Wang et al., 2022; Wang et al., 2019), boosting the possibility of better constraining the carbon cycle at finer spatial scale(Byrne et al., 2019). Byrne et al. (2019) explored the spatial scales of interannual variability of NEE constrained using GOSAT XCO_2, giving correlations between interannual variability at different scales and multiple "proxies", but the spatial scales at which the inversion results are robust remain unclear.

Here, we assimilate GOSAT XCO_2 observations using the time-dependent Bayesian synthesis method ("Method") to optimize terrestrial ecosystem carbon exchange (NEE) of 51 land regions (Figure S1a) from multiple TBMs. The inversion is from May 2009 to 2014, the first 20 month-period is treated as the spin-up stage, and the inversion results from 2011 to 2014 were analysed in this study. NEEs simulated from 12 TBMs were used as prior fluxes within the same atmospheric inversion framework and constrained with the same observations to explore on what scales the GOSAT XCO_2 retrievals can provide robust NEE estimates.

2 Methods

2.1 Inversion method

We use the time-dependent Bayesian synthesis method(Rayner et al., 1999), and the GOSAT XCO_2 retrievals, to estimate global surface CO_2 net fluxes. The key of this method is to minimize the following cost function(Rayner et al., 1999):

$$J = \frac{1}{2}(\boldsymbol{Ms} - \boldsymbol{c})^{\boldsymbol{T}}\boldsymbol{R}^{-1}(\boldsymbol{Ms} - \boldsymbol{c}) + \frac{1}{2}(\boldsymbol{s} - \boldsymbol{s_p})^{\boldsymbol{T}}\boldsymbol{Q}^{-1}(\boldsymbol{s} - \boldsymbol{s_p}) \quad (1)$$

where **M** is the transport operator; **c** is the observations; **s** is the vector of carbon flux combined with initial well-mixed atmospheric CO_2 concentration; $\mathbf{s_p}$ is a priori estimation of **s**; and **R** and **Q** are the uncertainties of **c** and $\mathbf{s_p}$, respectively. By minimizing this cost function, the posterior fluxes $\boldsymbol{s}_{post}$ and their uncertainties $\mathbf{Q}_{post}$ could be obtained as:

$$\boldsymbol{s}_{post} = (\boldsymbol{M}^T\boldsymbol{R}^{-1}M + \boldsymbol{Q}^{-1})^{-1}\left(\boldsymbol{M}^T\boldsymbol{R}^{-1}\boldsymbol{c} + \boldsymbol{Q}^{-1}\boldsymbol{s_p}\right) \quad (2)$$

$$\boldsymbol{Q}_{post} = (\boldsymbol{Q}^{-1} + \boldsymbol{M}^T\boldsymbol{R}^{-1}\boldsymbol{M})^{-1} \quad (3)$$

The global surface is separated into 69 regions, including 51 regions for land, and 18 regions for ocean (Figure S1a). The partition scheme of land was adopted from Wang et al. (2021). The bias-corrected GOSAT ACOS V7.3 XCO_2 for the years 2009-2014 is adopted as observations(Crisp et al., 2012; O'Dell et al., 2012; Wunch et al., 2011), and has been re-grided to 1°× 1° by Jiang et al. (2021) with the best quality approach(Wang et al., 2019).

Four types of a priori carbon fluxes were used in the inversion, namely terrestrial ecosystem carbon flux (NEE), ocean (OCEAN) carbon exchange, fossil fuel and cement production (FFC) carbon emissions, and biomass burning (FIRE) carbon emissions. The

OCEAN flux, FFC and FIRE emissions were adopted from the product of NOAA's CarbonTracker, version 2017 (CT2017). In many offshore areas, the OCEAN fluxes are missing, we filled them with the fluxes of 2009 simulated by the global ocean circulation and biogeochemistry model (OPA-PISCES–T)(Buitenhuis et al., 2006; Jiang et al., 2013). The prior NEE fluxes were obtained from 12 TBMs, including BEPS(Chen et al., 1999; Ju et al., 2006), CASA(Potter et al., 1993), and 10 models from TRENDYv9(Friedlingstein et al., 2020) (i.e., CABLE-POP(Haverd et al., 2018), DLEM(Tian et al., 2015), ISAM(Meiyappan et al., 2015), LPX-Bern(Lienert & Joos, 2018), OCN(Zaehle & Friend, 2010), ORCHIDEE(Lurton et al., 2020), ORCHIDEEv3(Vuichard et al., 2019), SDGVM(Walker et al., 2017), VISIT(Kato et al., 2013), YIBs(Yue & Unger, 2015)). BEPS is a satellite-based TBM, which was driven by the LAI and clumping index products from MODIS. In this study, the BEPS simulations were adopted from Jiang et al. (2021). The CASA simulations were also derived from CT2017. There are 10 TBMs in TRENDYv9 S3 simulations, we selected the simulations with spatial resolution greater than 1°×1°.

The transport operator **M** is simulated using the Model for Ozone And Related chemical Tracers, version 4 (MOZART-4)(Emmons et al., 2010). The MOZART-4 model was run at a spatial resolution of approximately 2.8°×2.8° (128 × 64 grids), and 28 vertical layers. It was driven by the ERA-Interim reanalysis data obtained from the European Centre for Medium-Range Weather Forecasts (ECMWF)(Dee et al., 2011). Using MOZART-4, we calculated the contributions of each month and each region to the XCO_2 at each grid and time. Following Jiang et al. (2013), for each month and each region, the model is continuously run for three years, with 1 Pg carbon emitted in the first month and no emission in the months thereafter. the spatial distribution of emissions within each land region was assigned according to the multi-year averaged net primary production (NPP), for the ocean region, no distribution was considered. The background CO_2 concentration was set to 390 ppm, which is the averaged concentration of April and May 2009 observed at the global background station of Mauna Loa (Ed Dlugokencky and Pieter Tans, NOAA/GML (gml.noaa.gov/ccgg/trends/)). The simulated XCO_2 contribution per month *t* and per region *i* were calculated based on a satellite averaging kernel according to the following equation(Connor et al., 2008):

$$XCO_2^{m,t,i} = \sum_j h_j k_j (A(x_{t,i}) - y_{a,j}) \quad (4)$$

where j represents the GOSAT XCO_2 retrieval layer, x is the simulated CO_2 profile, $A(x)$ is the mapping matrix, and h_j k_j, $y_{a,j}$ are the pressure weighting function, satellite kernel function, and a priori CO_2 profile provided by the GOSAT product, respectively. The OCEAN flux, FFC and FIRE emissions were assumed to be prescribed, and thus the CO_2 concentrations from the contributions of these three types of fluxes also simulated using the MOZART-4 model were pre-subtracted in the inversion system. Hence, the matrix *c* in eq. (1) can be further expressed as

$$c = c_{obs} - XCO_2^a - \sum_j h_j k_j (A(x_{t,i,FFC} + x_{t,i,FIRE}) - y_{a,j}) \quad (5)$$

where c_{obs} is the GOSAT XCO_2, XCO_2^a is the prior XCO_2 provided along the XCO_2 product. In order to save computational costs and reduce the size of the transport matrix **M**, the observations and the variables corresponding to the observations were rescaled to a resolution of 15°x15° per month in this paper.

For the uncertainties of prior fluxes, we assumed a global land uncertainty of 2.0 PgC yr^{-1}, which was distributed to different regions based on a multi-year average annual NPP from the CASA model(Potter et al., 1993). Considering that NPP is very small in winter and large in summer, assigning uncertainty exactly according to the monthly variation in NPP would result in little uncertainty in winter, so we adopted the scheme of averaging NPP with and without monthly variation and using this result to assign uncertainty. In addition, we fixed the lowest monthly uncertainty of each region to 0.1 PgC. The annual uncertainty of global land is within the range of previous studies(Baker et al., 2006; Basu et al., 2013; Deng & Chen, 2011; Houweling et al., 2004; Rodenbeck et al., 2003). We neglected the temporal and spatial correlation of the prior flux uncertainties. The observation error is 1.9 times of the retrieval error provided by the GOSAT product, which is the same as Jiang et al. (2021). The observations were also averaged over a 15°×15° grid for each month, and the minimum observation error was set to 1 ppm. For the inversion results, May 2009-December 2010 is taken as the spin-up phase, and only the inversion results from 2011-2014 are analyzed and discussed.

We performed two sensitivity experiments using different a priori flux uncertainty and observation error settings To investigate the impact of prior uncertainty settings on the inversion results, we conducted a sensitive experiment in which the prior uncertainty of each land region was set to be the standard deviation of the 12 prior NEEs (Philip et al., 2019), and the rest of the settings were kept consistent with Base Case, referred to as Case Q. To explore the effect of observation error on the estimation results, we set up a sensitivity experiment, ignoring the difference in observation errors, by setting the observation error uniformly at 0.5 ppm, which may be the accuracy goal for future satellite observations(Sierk et al., 2021), and then scaling them up by a factor of 1.9, keeping the rest of the settings consistent with Base Case, called Case R.

2.2 Evaluation data and method

In this study, surface CO_2 observations from the CO_2 GLOBALVIEWplus v7.0 ObsPack dataset(Cox et al., 2021) are used for independent evaluations. We selected 168 sets of discrete (flask), and quasi-continuous (in-situ) measurements at surface and tower with observation start date earlier than 2011, and stop date later than 2014. Of these, there are 34, 37, 75, 4, 9 and 9 sets of records available for Asia, Europe, North America, S. America, Africa, and Oceania, respectively. In addition, in Asia, the ObsPack observations are mainly distributed in the middle and high latitudes. Therefore, we further chose the observations from the Comprehensive Observation Network for Trace gases by Airliner (CONTRAIL) project(Machida et al., (Reference date: 2021/10/29), 2018; Machida et al., 2008; Matsueda et al., 2008; Matsueda et al., 2015) to evaluate the posterior CO_2 over Southeast Asia. The CONTRAIL project measures CO_2 concentrations on two passenger aircrafts along their flight paths. Vertical profiles of CO_2 concentrations near airports were observed during the taking off and landing. We selected observations between 2000 m to 6000 m heights, since the CO_2 concentrations below 2000m could be highly influenced by airport pollution, and above 6000 m CO_2 are fully mixed. At the heights of 2000m to 6000m, every 500 m was divided into one layer, and in each layer, the observations were averaged and compared with the simulations.

Two forward simulations from May 2009 to Dec 2014 using the MOZART-4 model and the prior and posterior fluxes of the 12 TBMs were conducted to create prior and posterior CO_2 concentrations, respectively. The initial field at 00:00 UTC May 01, 2009 is obtained from the

reanalysis concentration of Carbon Tracker CT2019B (CT2019B)(Jacobson et al., 2020). The mean deviation (BIAS) and root mean square error (RMSE) were used as reference indicators for the evaluation results. The monthly mean BIAS and RMSE at each continent were calculated.

3 Results

3.1 Uncertainty reductions on different spatial scales

Generally, there are big differences in the NEE simulated using different TBMs(Monteil et al., 2020). In this study, 12 TBMs (see Methods) were used as prior fluxes. The NEE of these 12 TBMs also has large differences. On the global scale, the mean annual NEEs from 2011 to 2014 are in the range of -2.66 (CASA model) to -9.97 (LPX-Bern model) PgC yr^{-1} (Figure S2). We treat the standard deviation of the 12 TBMs' NEE as the 1-σ uncertainty, and the mean of the 12 TBMs as the best estimate of NEE for one region. To explore the spatial scales at which GOSAT XCO_2 retrievals can provide robust NEE estimates, we analyse the relative prior uncertainty and uncertainty reduction rate (URR) after constraints at the global scale, the hemispheric scale (northern mid to high latitudes, tropical latitudes, southern middle latitudes), the continental scale, the half of continental scale (1/2 continent), the quarter of continental scale (1/4 continent), and small regions. The definition of the hemispheric scale and the latter three scales is given in Figure S1b-d.

Figure 1 shows the relative uncertainties of the prior and posterior NEEs and their URRs after constraint using GOSAT XCO_2 on different spatial scales. Clearly, the relative prior uncertainty increases with decreasing spatial scale. On the global scale, the relative prior uncertainty is about 40%; on the continent, 1/2 continent, and 1/4 continent scales, the mean relative prior uncertainties are 47%, 53%, and 54%, respectively. On small regions (51 regions for global land, same thereafter), the mean relative prior uncertainty reaches 61%, with a range from 29% to 345%, and the Figure S3 presents relative a priori uncertainty views for small regions. The continent-scale relative prior uncertainty ranges from 36% to 88%, with 46%, 50%, 48%, 36%, 48% and 88% for Asia, North America, Europe, South America, Africa and Australia respectively.

After being constrained by the GOSAT XCO_2 retrievals, the uncertainty of the posterior NEE is substantially reduced. We find that the URR is significantly related to the spatial scale. The larger the spatial scale, the larger the URR, and vice versa. From the whole globe to the mean of 51 regions, the URR decreases from 85% to 19%. On the continental scale, the mean URR is 60%. N. America has the largest URR, with a value of 85%, followed by Asia (75%), S. America (64%) and Australia (50%), and Europe has the smallest URR, with a value of only 41%. On small regions, posterior uncertainty decreased in most regions (0 to 55%), except for 6 regions (located in northern Asia, eastern North America, Amazonia, and Southeast Asia) where posterior uncertainty increased to some extent (3% to 48%), which may be related to the settings of prior uncertainty and observation errors (Figure S4). Moreover, the relative posterior uncertainty is lower than the prior on global to ¼ continental scales, while in small regions, the relative posterior uncertainty is comparable to the prior. This suggests that the GOSAT XCO_2 retrievals can constrain the terrestrial's NEE well at the continental scale, but has limited ability to constrain carbon fluxes at subcontinental or smaller scales, implying that the inversion results on sub-continental scales are highly related to the adopted prior NEE.

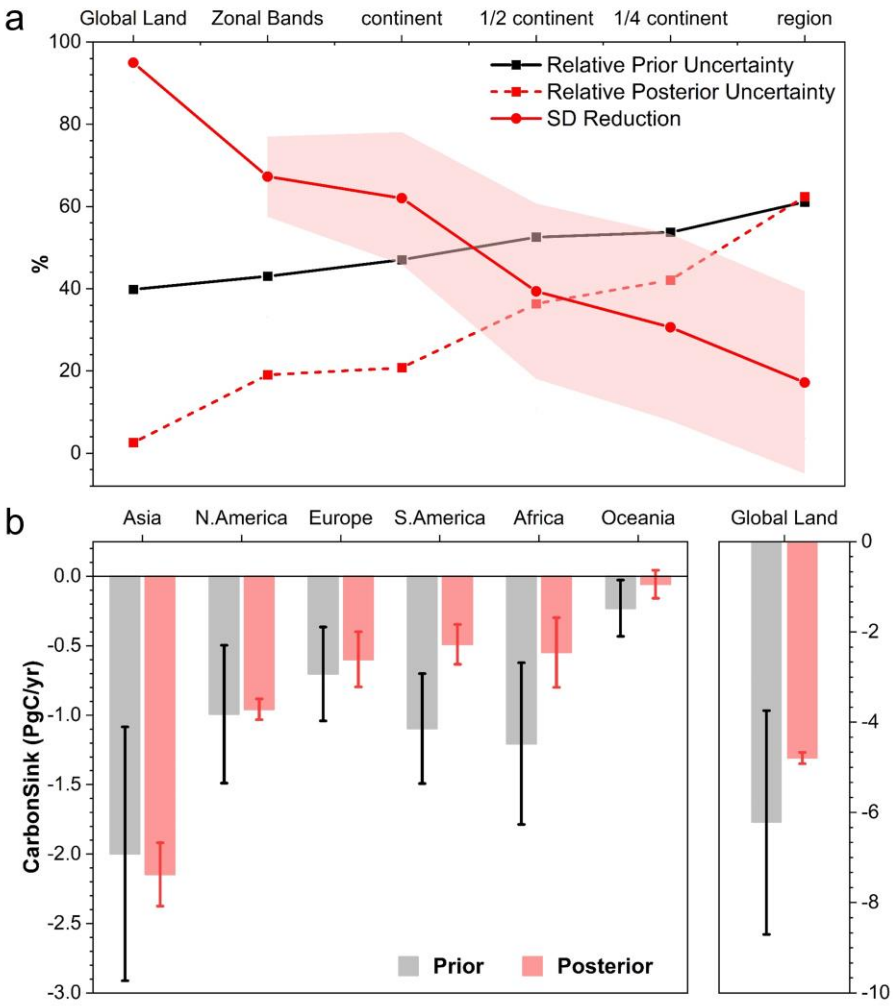

Figure 1. Uncertainty at different scales and terrestrial carbon sink on the continental scale. (**a**) Relative uncertainties of the prior and posterior fluxes and uncertainty reduction rates after constrained using GOSAT XCO_2 in different spatial scales, and (**b**) annual prior and posterior NEEs on the global and continental scales. The uncertainty is depicted as the standard deviation of the simulated NEEs by the 12 TBMs.

3.2 Annual and seasonal cycles of NEE on the continental scale

As mentioned above, on the continental scale, the posterior fluxes converge significantly. For prior fluxes, in Asia, N. America, Europe, S. America, Africa, and Australia, their averaged NEEs during the study period are in the range of -0.25 to -3.27, -0.13 to -1.76, -0.24 to -1.26, -0.29 to -1.62, -0.31 to -2.14, and -0.01 to -0.69 PgC yr^{-1}, with mean of -2.00±0.91, -0.99±0.50, -0.70±0.34, -1.10±0.40, -1.20±0.58, and -0.23±0.21 PgC yr^{-1}, respectively. After constraining using XCO_2 retrievals, we obtain the mean NEEs of -2.15±0.23, -0.96±0.07, -0.60±0.20, -0.55±0.25, -0.49±0.14, and -0.06±0.1 PgC yr^{-1}, respectively.

We further explore whether the seasonal cycles of continental-scale NEE also converged significantly. As shown in Figure 2, for the prior fluxes, the monthly NEEs of different TBMs varies largely in all continents. In Asia, Europe, and N. America, although all models show

strong land carbon sinks in warm seasons (May to September), and clear land carbon sources during the cold seasons, however, the seasonal magnitudes vary significantly across models, which are in the range of 0.39 to 2.88 PgC mo^{-1}, 0.29 to 1.41 PgC mo^{-1}, and 0.17 to 1.92 PgC mo^{-1}, respectively, with corresponding mean seasonal magnitudes of 1.34±0.62, 0.81±0.26, 0.96±0.44 PgC mo^{-1}. Moreover, in Africa, S. America, and Australia, the different TBMs show very inconsistent seasonal cycles. For example, in Australia, some models show carbon sinks from April to October, some models show the opposite, and there are individual models that show carbon sinks throughout the year. The mean seasonal magnitudes of Africa, S. America, and Australia are 0.38±0.13, 0.51±0.29, and 0.19±0.16 PgC mo^{-1}, respectively.

For the posterior fluxes, the seasonal cycles of different TBMs are in a narrow spread. Compared to the prior magnitudes, the posterior magnitudes have increased in Asia, N. America, Europe, and Africa, with Africa in particular more than doubling, while in S. America and Australia, they have decreased. The mean seasonal magnitudes of Asia, N. America, Europe, Africa, S. America, and Australia are 1.30±0.21, 1.06±0.12, 0.90±0.13, 0.39±0.08, 0.32±0.08, and 0.13±0.07 PgC mo^{-1}, respectively. Uncertainties of their magnitudes are reduced by a range from 34 to 73%. In addition to more unified amplitudes, basically all TBMs also present a consistent phase in their seasonal cycle. Particularly, in the prior NEEs, there are individual models whose results deviate significantly from others. For example, in Asia, North America, and Europe, one model shows abnormally high sources in autumn, and in S. America and Australia, there is a model showing abnormally high sources in June-October. After constraint by GOSAT observations, these anomalies of individual patterns disappear.

When comparing the multi-model mean prior and posterior seasonal cycles, in Asia, Europe, and North America, the posterior seasonal cycle is consistent with the prior results, but the carbon sink is stronger in summer and the carbon source is stronger in autumn. In Africa, South America, and Australia, the posterior and prior seasonal cycles are quite different. In Africa, the prior NEEs show carbon sinks throughout the year, with the strongest carbon sinks in July-August and the weakest sinks in February and November; while the posterior NEE shows that there are significant carbon sources from March to June and from October to November, and significant carbon sinks in December-January and July-September, with the strongest sink in August. In South America, the prior NEEs show a unimodal distribution, with the strongest sink and source in January and September, respectively; but the posterior results show that the carbon sink increases significantly in every month except August-September, and the months with stronger sources appear in June and September. In Australia, the prior NEEs show carbon sinks from December to May, with the strongest in March, and carbon sources from June to November, with the strongest in October; while the posterior NEE shows a significant increase in carbon sources from November to June, and an obvious decrease from August to October, displaying a double-peak and double-valley pattern.

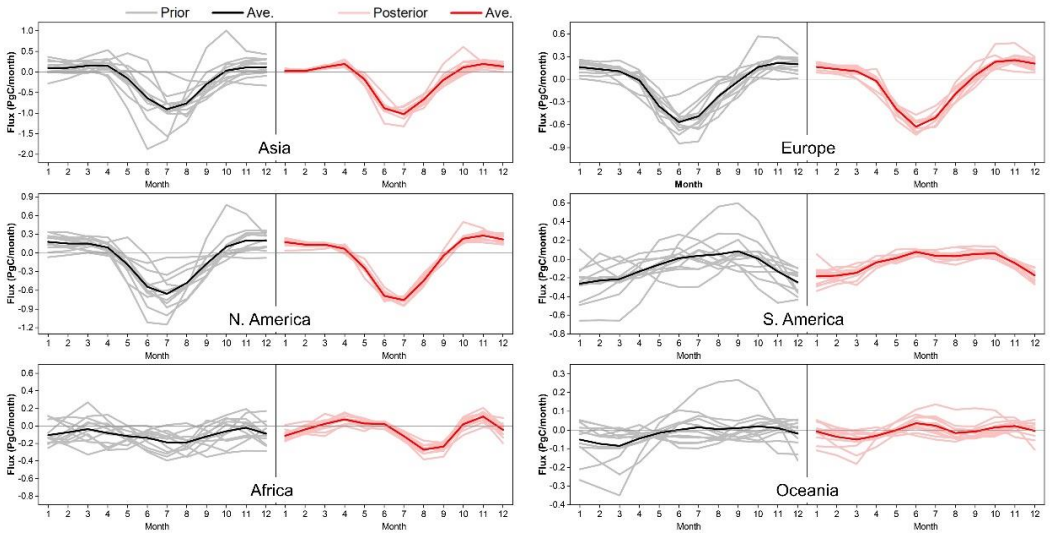

Figure 2 Averaged prior and posterior seasonal cycle of NEE in different continents during 2011-2014. The lighter lines correspond to the NEEs of different TBMs, and the darker lines represent the multiple models mean.

3.3 Evaluation for the inversion results

We evaluated the inversion results using independent surface CO_2 observations over the globe. Figure 3 shows the continental averaged monthly mean observed CO_2 concentrations and the 12 TBMs averaged prior and posterior CO_2 concentrations. Compared to the prior CO_2 concentrations, except for Asia, the posterior concentrations are much closer to the observed values over all continents. The root mean square error (RMSE) between the observations and simulations in Europe, N. America, S. America, Africa, and Australia decrease from a priori of 2.32, 2.58, 2.45, 1.96, and 1.80 ppm to a posteriori of 1.43, 1.51, 1.00, 0.72, and 0.57 ppm, respectively, with reduction rates of RMSE in the range of 40% ~ 68%. For the individual models (Figure S5), the mean bias (BIAS) and RMSE of the posterior CO_2 are also lower than those of the prior CO_2 for almost all models and in all the continents. Generally, the prior CO_2 of the LPX-Bern, ORCHIDEE, ORCHIDEEv3, SDGVM, and VISIT models have larger RMSE than the other models in all continents. After being constrained with XCO_2 data, the posterior CO_2 RMSE of these 5 models are similar with those of the others. In Asia, for the prior CO_2 concentrations, there are about half of the models with negative biases, and the rest with positive biases, with values in the range of -4.29 ~ 5.27 ppm, which results in a very small BIAS in the mean prior CO_2 of -0.08 ppm, while for the posterior CO_2, almost all models have small positive biases, with values in the range of -0.72 ~ 2.35 ppm and average bias of 1.20 ppm. In Southeast Asia, compared with the aircraft observations, the prior CO_2 have large negative bias (about -3 ppm), while the posterior CO_2 have a much smaller bias, with a value about -1 ppm (Figure S6). This indicates that the inversion results in Asia of all TBMs are also improved.

It can be found that the posterior CO_2 in Asia agrees well with the observation in summer, but in winter, the posterior concentration is higher than the observation, indicating that the carbon source in Asia was overestimated in winter. Although the posterior concentrations in N. America and Europe match the observations better overall, similar characteristics to Asia were observed, i.e., the differences between the posterior concentrations and the observations are

greater in winter than in summer, suggesting it might be caused by poor observations in winter (Figure S7).

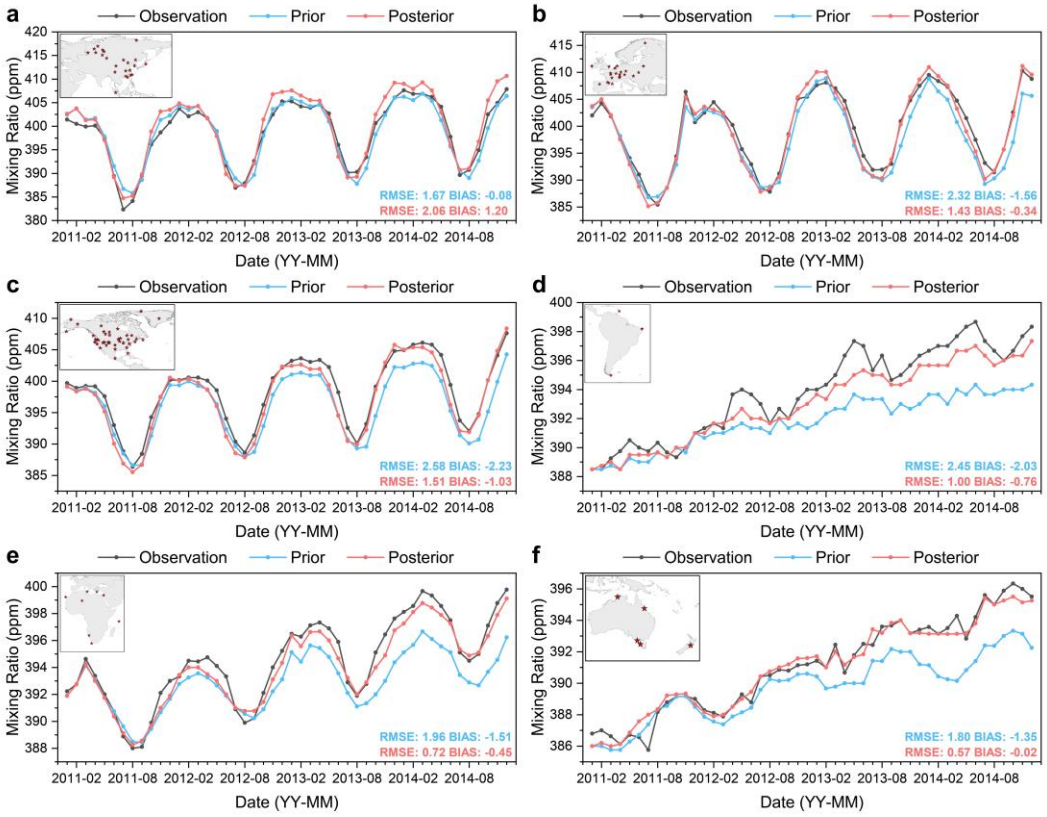

Figure 3 Time series of modeled and observed monthly mean CO_2 concentrations for **a**, Asia, **b**, Africa, **c**, N. America, **d**, S. America, **e**, Europe, and **f**, Oceania. The embedded map in the upper left corner shows the location of the stations used in each continent.

4 Discussion and conclusion

With NEEs from 12 different TBMs, our work produces a robust estimate at the continental scale using GOSAT XCO_2, with very consistent annual mean carbon fluxes and seasonal cycles. The assessment of the results by independent observations shows that the posteriori concentrations are closer to the observations. Compared to previous estimates, the estimated net biosphere exchanges (NBE, =NEE+FIRE) in N. America, Europe, S. America, Africa, and Australia are close to or between the estimates of GCAS2021 (Jiang et al., 2022) and CMS-Flux NBE 2020 (Liu et al., 2021) during the same period (Figure S8), which were inferred from the same satellite retrievals as this study; while in Asia, the land sink of this study is significantly stronger than both. Compared to the NBEs constrained using surface air-sample measurements (i.e., CT2019B, Jacobson et al., 2020; Jena CarboScope s10oc_v2020, Rodenbeck et al., 2018; CAMS v18r2, Chevallier et al., 2010) (Figure S8), in Asia, N. America, and Europe, our results are in the range of these three estimates, while in S. America, we show a stonger land sink, and in Afirca and Australia, we show a stonger source. For the Asia's NEE, it is also comparable to the estimate of Zhang et al. (2014), who used Asia's ground and aircraft observations as many as possible, and less than the estimate based on eddy covariance measurements (Ichii et al., 2017). Compared to the state-of-the-art bottom up estimate for the

period of 2000-2009 (Ciais et al., 2021) , this study shows a stronger sink in N. America, EuroAsia, and S. America, but a weaker one in Africa and Australia. On globe land, the NEE is reduced from a priori of -6.22±2.48 PgC yr^{-1} to a posteriori of -4.79±0.12 PgC yr^{-1}. Combined with the prescribed fluxes of ocean (-2.45 PgC yr^{-1}), fire (1.93 PgC yr^{-1}), and fossil fuel and cement (9.68 PgC yr^{-1}), the posterior global net flux to the atmosphere is 4.37 PgC yr^{-1}, which is very close to the observed mean atmospheric CO_2 growth rate of 4.51 PgC yr^{-1} (Friedlingstein et al., 2020).

The setting of prior uncertainties and observation errors can affect the estimates of NEE. When using the standard deviations of the 12 TBMs as the prior uncertainties in each region (Case Q, as described in 'Method'), the URRs in most regions of high and low latitudes are lower than those of the Base case. The reason is that with this scheme, the given uncertainty for each prior flux at high latitude regions is greater, that is, for each prior flux, the degree of adjustment freedom has increased, but the observation constraint is insufficient in this area, thus the convergence of the 12 NEEs has become poorer; on the contrary, the prior uncertainty in the tropics has become smaller, and there are relatively more observations, as a result, the range that each prior flux can be adjusted is reduced, and the convergence of the 12 NEEs is also reduced (Figure S4 and Figure S9). Besides, we also find a significant increase of URR in the tropical regions of Amazon and Indochina, indicating that a suitable prior uncertainty setting is very important. On the continental scale, the URRs decrease on all continents except Europe, while the estimated NEE in all continents do not change much compared with the Base case (Figure S10). When using a uniform and much smaller observation error (Case R, as described in 'Method'), the URRs have increased in most regions, especially at high latitudes (Figure S4). Overall, the different prior uncertainty and observation error settings do not change the situation that URR decreases significantly as the spatial scale decreases, but with the different prior uncertainty setting, the decrease is more rapid, while with small observation error, the decline rate is reduced. In Case R, the URR of 1/4 continent could reach more than 40%, and that of the 51 regions mean reaches about 25% (Figure S11). We conclude that currently, the GOSAT XCO_2 can only give a robust estimate of the carbon flux on the continental scale, and under the current satellite observing capacity, improving the XCO_2 accuracy can effectively reduce the spatial scale of robust carbon flux estimates.

Acknowledgments

This work is supported by the National Key R&D Program of China (Grant No: 2020YFA0607504), Fengyun Application Pioneering Project (Grant No: FY-APP-2022.0505), the Research Funds for the Frontiers Science Center for Critical Earth Material Cycling, Nanjing University (Grant No: 090414380031), and the National Natural Science Foundation of China (Grant No. 41907378). We acknowledge all atmospheric data providers to obspack_CO_2_1_GLOBALVIEWplus_ v7.0_2021-08-18. CarbonTracker CT2019B results provided by NOAA ESRL, Boulder, Colorado, USA from the website at

http://carbontracker.noaa.gov. The GOSAT data are produced by the OCO project at the Jet Propulsion Laboratory, California Institute of Technology, and obtained from the data archive at the NASA Goddard Earth Science Data and Information Services Center. We are also grateful to the High-Performance Computing Center (HPCC) of Nanjing University for doing the numerical calculations in this paper on its blade cluster system.

Data Availability Statement

The ACOS 7.3 Level 2 Lite data set of GOSAT XCO2 column concentrations is publicly available at https://oco2.gesdisc.eosdis.nasa.gov/opendap/ACOS_L2_Lite_FP.7.3/contents.html. The TRENDY TBMs data are available at https://sites.exeter.ac.uk/trendy. The CarbonTracker CT2017 fluxes used as prior information in the model simulations can be accessed from the website https://gml.noaa.gov/aftp/products/carbontracker/co2/CT2017. The ObsPack data can be downloaded from https://gml.noaa.gov/ccgg/obspack/data.php. The CONTRAIL data can be obtained from the ObsPack dataset. The monthly carbon fluxes for the 51 terrestrial regions estimated in this study are available at https://doi.org/10.5281/zenodo.7090590.

Conflict of Interest

The authors declare no conflicts of interest relevant to this study.

References

Baker, D. F., Bösch, H., Doney, S. C., O'Brien, D., & Schimel, D. S. (2010). Carbon source/sink information provided by column CO_2 measurements from the Orbiting Carbon Observatory. *Atmospheric Chemistry and Physics*, *10*(9), 4145-4165. https://doi.org/10.5194/acp-10-4145-2010

Baker, D. F., Law, R. M., Gurney, K. R., Rayner, P., Peylin, P., Denning, A. S., et al. (2006). TransCom 3 inversion intercomparison: Impact of transport model errors on the interannual

variability of regional CO_2 fluxes, 1988-2003. *Global Biogeochemical Cycles*, *20*(1). https://doi.org/10.1029/2004GB002439

Basu, S., Guerlet, S., Butz, A., Houweling, S., Hasekamp, O., Aben, I., et al. (2013). Global CO_2 fluxes estimated from GOSAT retrievals of total column CO_2. *Atmospheric Chemistry and Physics*, *13*(17), 8695-8717. https://doi.org/10.5194/acp-13-8695-2013

Buitenhuis, E., Le Quere, C., Aumont, O., Beaugrand, G., Bunker, A., Hirst, A., et al. (2006). Biogeochemical fluxes through mesozooplankton. *Global Biogeochemical Cycles*, *20*(2). https://doi.org/10.1029/2005GB002511

Byrne, B., Jones, D. B. A., Strong, K., Polavarapu, S. M., Harper, A. B., Baker, D. F., & Maksyutov, S. (2019). On what scales can GOSAT flux inversions constrain anomalies in terrestrial ecosystems? *Atmospheric Chemistry and Physics*, *19*(20), 13017-13035. https://doi.org/10.5194/acp-19-13017-2019

CarbonTracker, T. (2018). CarbonTracker CT2017. In: NOAA Earth System Research Laboratory, Global Monitoring Division.

Chen, J. M., Liu, J., Cihlar, J., & Goulden, M. L. (1999). Daily canopy photosynthesis model through temporal and spatial scaling for remote sensing applications. *Ecological Modelling*, *124*(2-3), 99-119. https://doi.org/10.1016/S0304-3800(99)00156-8

Chevallier, F., Ciais, P., Conway, T. J., Aalto, T., Anderson, B. E., Bousquet, P., et al. (2010). CO_2 surface fluxes at grid point scale estimated from a global 21 year reanalysis of atmospheric measurements. *Journal of Geophysical Research-Atmospheres*, *115*. https://doi.org/10.1029/2010JD013887

Chevallier, F., Palmer, P. I., Feng, L., Boesch, H., O'Dell, C. W., & Bousquet, P. (2014). Toward robust and consistent regional CO_2 flux estimates from in situ and spaceborne measurements of

atmospheric CO_2. *Geophysical Research Letters, 41*(3), 1065-1070. https://doi.org/10.1002/2013GL058772

Ciais, P., Yao, Y., Gasser, T., Baccini, A., Wang, Y., Lauerwald, R., et al. (2021). Empirical estimates of regional carbon budgets imply reduced global soil heterotrophic respiration. *National Science Review, 8*(2). https://doi.org/10.1093/nsr/nwaa145

Connor, B. J., Boesch, H., Toon, G., Sen, B., Miller, C., & Crisp, D. (2008). Orbiting carbon observatory: Inverse method and prospective error analysis. *Journal of Geophysical Research-Atmospheres, 113*(D5). https://doi.org/10.1029/2006JD008336

Cox, A., Di Sarra, A. G., Vermeulen, A., Manning, A., Beyersdorf, A., Zahn, A., et al. (2021). *Multi-laboratory compilation of atmospheric carbon dioxide data for the period 1957-2020; obspack_CO_2_1_GLOBALVIEWplus_v7.0_2021-08-18*. Retrieved from: http://www.esrl.noaa.gov/gmd/ccgg/obspack/data.php?id=obspack_CO_2_1_GLOBALVIEWplus_v7.0_2021-08-18

Crisp, D., Fisher, B. M., O'Dell, C., Frankenberg, C., Basilio, R., Bösch, H., et al. (2012). The ACOS CO_2 retrieval algorithm – Part II: Global XCO_2 data characterization. *Atmospheric Measurement Techniques, 5*(4), 687-707. https://doi.org/10.5194/amt-5-687-2012

Crowell, S., Baker, D., Schuh, A., Basu, S., Jacobson, A. R., Chevallier, F., et al. (2019). The 2015–2016 carbon cycle as seen from OCO-2 and the global in situ network. *Atmospheric Chemistry and Physics, 19*(15), 9797-9831. https://doi.org/10.5194/acp-19-9797-2019

Dee, D. P., Uppala, S. M., Simmons, A. J., Berrisford, P., Poli, P., Kobayashi, S., et al. (2011). The ERA-Interim reanalysis: configuration and performance of the data assimilation system. *Quarterly Journal of the Royal Meteorological Society, 137*(656), 553-597. https://dx.doi.org/10.1002/qj.828

Deng, F., & Chen, J. M. (2011). Recent global CO_2 flux inferred from atmospheric CO_2 observations and its regional analyses. *Biogeosciences, 8*(11), 3263-3281. https://doi.org/10.5194/bg-8-3263-2011

Deng, F., Jones, D. B. A., Henze, D. K., Bousserez, N., Bowman, K. W., Fisher, J. B., et al. (2014). Inferring regional sources and sinks of atmospheric CO_2 from GOSAT XCO_2 data. *Atmospheric Chemistry and Physics, 14*(7), 3703-3727. https://doi.org/10.5194/acp-14-3703-2014

Emmons, L. K., Walters, S., Hess, P. G., Lamarque, J. F., Pfister, G. G., Fillmore, D., et al. (2010). Description and evaluation of the Model for Ozone and Related chemical Tracers, version 4 (MOZART-4). *Geoscientific Model Development, 3*(1), 43-67. https://doi.org/10.5194/gmd-3-43-2010

Friedlingstein, P., O'Sullivan, M., Jones, M. W., Andrew, R. M., Hauck, J., Olsen, A., et al. (2020). Global Carbon Budget 2020. *Earth System Science Data, 12*(4), 3269-3340. https://doi.org/10.5194/essd-12-3269-2020

Gurney, K. R., Law, R. M., Denning, A. S., Rayner, P. J., Baker, D., Bousquet, P., et al. (2002). Towards robust regional estimates of CO_2 sources and sinks using atmospheric transport models. *Nature, 415*(6872), 626-630. https://doi.org/10.1038/415626a

Haverd, V., Smith, B., Nieradzik, L., Briggs, P. R., Woodgate, W., Trudinger, C. M., et al. (2018). A new version of the CABLE land surface model (Subversion revision r4601) incorporating land use and land cover change, woody vegetation demography, and a novel optimisation-based approach to plant coordination of photosynthesis. *Geoscientific Model Development, 11*(7), 2995-3026. https://doi.org/10.5194/gmd-11-2995-2018

Houweling, S., Breon, F. M., Aben, I., Rodenbeck, C., Gloor, M., Heimann, M., & Ciais, P. (2004). Inverse modeling of CO_2 sources and sinks using satellite data: a synthetic inter-comparison of measurement techniques and their performance as a function of space and time. *Atmospheric Chemistry and Physics*, *4*, 523-538. https://doi.org/10.5194/acp-4-523-2004

Ichii, K., Ueyama, M., Kondo, M., Saigusa, N., Kim, J., Alberto, M. C., et al. (2017). New data-driven estimation of terrestrial CO_2 fluxes in Asia using a standardized database of eddy covariance measurements, remote sensing data, and support vector regression. *Journal of Geophysical Research-Biogeosciences*, *122*(4), 767-795. https://doi.org/10.1002/2016JG003640

Jacobson, A. R., Schuldt, K. N., Miller, J. B., Oda, T., Tans, P., Arlyn, A., et al. (2020). CarbonTracker CT2019B. In: NOAA Global Monitoring Laboratory, *Global Monitoring Division*, https://doi.org/10.25925/20201008

Jiang, F., Ju, W., He, W., Wu, M., Wang, H., Wang, J., et al. (2022). A 10-year global monthly averaged terrestrial net ecosystem exchange dataset inferred from the ACOS GOSAT v9 XCO_2 retrievals (GCAS2021). *Earth System Science Data*, *14*(7), 3013-3037. https://doi.org/10.5194/essd-14-3013-2022

Jiang, F., Wang, H., Chen, J. M., Ju, W., Tian, X., Feng, S., et al. (2021). Regional CO_2 fluxes from 2010 to 2015 inferred from GOSAT XCO_2 retrievals using a new version of the Global Carbon Assimilation System. *Atmospheric Chemistry and Physics*, *21*(3), 1963-1985. https://doi.org/10.5194/acp-21-1963-2021

Jiang, F., Wang, H. W., Chen, J. M., Zhou, L. X., Ju, W. M., Ding, A. J., et al. (2013). Nested atmospheric inversion for the terrestrial carbon sources and sinks in China. *Biogeosciences*, *10*(8), 5311-5324. https://doi.org/10.5194/bg-10-5311-2013

Ju, W. M., Chen, J. M., Black, T. A., Barr, A. G., Liu, J., & Chen, B. Z. (2006). Modelling multi-year coupled carbon and water fluxes in a boreal aspen forest. *Agricultural and Forest Meteorology, 140*(1-4), 136-151. https://doi.org/10.1016/j.agrformet.2006.08.008

Kato, E., Kinoshita, T., Ito, A., Kawamiya, M., & Yamagata, Y. (2013). Evaluation of spatially explicit emission scenario of land-use change and biomass burning using a process-based biogeochemical model. *Journal of Land Use Science, 8*(1), 104-122. https://doi.org/10.1080/1747423X.2011.628705

Lienert, S., & Joos, F. (2018). A Bayesian ensemble data assimilation to constrain model parameters and land-use carbon emissions. *Biogeosciences, 15*(9), 2909-2930. https://doi.org/10.5194/bg-15-2909-2018

Liu, J., Baskaran, L., Bowman, K., Schimel, D., Bloom, A. A., Parazoo, N. C., et al. (2021). Carbon Monitoring System Flux Net Biosphere Exchange 2020 (CMS-Flux NBE 2020). *Earth System Science Data, 13*(2), 299-330. https://doi.org/10.5194/essd-13-299-2021

Lurton, T., Balkanski, Y., Bastrikov, V., Bekki, S., Bopp, L., Braconnot, P., et al. (2020). Implementation of the CMIP6 Forcing Data in the IPSL-CM6A-LR Model. *Journal of Advances in Modeling Earth Systems, 12*(4). https://doi.org/10.1029/2019MS001940

Machida, T., Ishijima, K., Niwa, Y., Tsuboi, K., Sawa, Y., Matsueda, H., & Andrae, U. ((Reference date: 2021/10/29), 2018). *Atmospheric CO_2 mole fraction data of CONTRAIL-CME, ver.2021.1.0*.

Machida, T., Matsueda, H., Sawa, Y., Nakagawa, Y., Hirotani, K., Kondo, N., et al. (2008). Worldwide Measurements of Atmospheric CO_2 and Other Trace Gas Species Using Commercial Airlines. *Journal of Atmospheric and Oceanic Technology, 25*(10), 1744-1754. https://doi.org/10.1175/2008JTECHA1082.1

Maksyutov, S., Takagi, H., Valsala, V. K., Saito, M., Oda, T., Saeki, T., et al. (2013). Regional CO_2 flux estimates for 2009–2010 based on GOSAT and ground-based CO_2 observations. *Atmospheric Chemistry and Physics, 13*(18), 9351-9373. https://doi.org/10.5194/acp-13-9351-2013

Matsueda, H., Machida, T., Sawa, Y., Nakagawa, Y., Hirotani, K., Ikeda, H., et al. (2008). Evaluation of atmospheric CO_2 measurements from new flask air sampling of JAL airliner observations. *Papers in Meteorology and Geophysics, 59*, 1-17. https://doi.org/10.2467/mripapers.59.1

Matsueda, H., Machida, T., Sawa, Y., & Niwa, Y. (2015). Long-term change of CO_2 latitudinal distribution in the upper troposphere. *Geophysical Research Letters, 42*(7), 2508-2514. https://doi.org/10.1002/2014GL062768

Meiyappan, P., Jain, A. K., & House, J. I. (2015). Increased influence of nitrogen limitation on CO_2 emissions from future land use and land use change. *Global Biogeochemical Cycles, 29*(9), 1524-1548. https://doi.org/10.1002/2015GB005086

Monteil, G., Broquet, G., Scholze, M., Lang, M., Karstens, U., Gerbig, C., et al. (2020). The regional European atmospheric transport inversion comparison, EUROCOM: first results on European-wide terrestrial carbon fluxes for the period 2006–2015. *Atmospheric Chemistry and Physics, 20*(20), 12063-12091. https://doi.org/10.5194/acp-20-12063-2020

O'Dell, C. W., Connor, B., Bosch, H., O'Brien, D., Frankenberg, C., Castano, R., et al. (2012). The ACOS CO_2 retrieval algorithm - Part 1: Description and validation against synthetic observations. *Atmospheric Measurement Techniques, 5*(1), 99-121. https://doi.org/10.5194/amt-5-99-2012

549 Peylin, P., Law, R. M., Gurney, K. R., Chevallier, F., Jacobson, A. R., Maki, T., et al. (2013).
550 Global atmospheric carbon budget: results from an ensemble of atmospheric CO_2 inversions.
551 *Biogeosciences, 10*(10), 6699-6720. https://doi.org/10.5194/bg-10-6699-2013
552 Philip, S., Johnson, M. S., Potter, C., Genovesse, V., Baker, D. F., Haynes, K. D., et al. (2019).
553 Prior biosphere model impact on global terrestrial CO_2 fluxes estimated from OCO-2 retrievals.
554 *Atmospheric Chemistry and Physics, 19*(20), 13267-13287. https://doi.org/10.5194/acp-19-
555 13267-2019
556 Potter, C. S., Randerson, J. T., Field, C. B., Matson, P. A., Vitousek, P. M., Mooney, H. A., &
557 Klooster, S. A. (1993). Terrestrial Ecosystem Production - a Process Model-Based on Global
558 Satellite and Surface Data. *Global Biogeochemical Cycles, 7*(4), 811-841.
559 https://doi.org/10.1029/93GB02725
560 Rayner, P. J., Enting, I. G., Francey, R. J., & Langenfelds, R. (1999). Reconstructing the recent
561 carbon cycle from atmospheric CO_2, delta C-13 and O-2/N-2 observations. *Tellus Series B-*
562 *Chemical and Physical Meteorology, 51*(2), 213-232.
563 https://doi.org/10.3402/tellusb.v51i2.16273
564 Rodenbeck, C., Houweling, S., Gloor, M., & Heimann, M. (2003). CO_2 flux history 1982-2001
565 inferred from atmospheric data using a global inversion of atmospheric transport. *Atmospheric*
566 *Chemistry and Physics, 3*, 1919-1964. https://doi.org/10.5194/acp-3-1919-2003
567 Rodenbeck, C., Zaehle, S., Keeling, R., & Heimann, M. (2018). How does the terrestrial carbon
568 exchange respond to inter-annual climatic variations? A quantification based on atmospheric
569 CO_2 data. *Biogeosciences, 15*(8), 2481-2498. https://doi.org/10.5194/bg-15-2481-2018
570 Sierk, B., Fernandez, V., Bézy, J. L., Meijer, Y., Durand, Y., Bazalgette Courrèges-Lacoste, G.,
571 et al. (2021). *The Copernicus CO_2M mission for monitoring anthropogenic carbon dioxide*

emissions from space. Paper presented at the International Conference on Space Optics — ICSO 2020. https://doi.org/10.1117/12.2599613

Thompson, R. L., Patra, P. K., Chevallier, F., Maksyutov, S., Law, R. M., Ziehn, T., et al. (2016). Top-down assessment of the Asian carbon budget since the mid 1990s. *Nature Communications, 7,* 10724. https://doi.org/10.1038/ncomms10724

Tian, H., Chen, G., Lu, C., Xu, X., Hayes, D. J., Ren, W., et al. (2015). North American terrestrial CO_2 uptake largely offset by CH4 and N2O emissions: toward a full accounting of the greenhouse gas budget. *Climatic Change*, *129*(3-4), 413-426. https://doi.org/10.1007/s10584-014-1072-9

Vuichard, N., Messina, P., Luyssaert, S., Guenet, B., Zaehle, S., Ghattas, J., et al. (2019). Accounting for carbon and nitrogen interactions in the global terrestrial ecosystem model ORCHIDEE (trunk version, rev 4999): multi-scale evaluation of gross primary production. *Geoscientific Model Development*, *12*(11), 4751-4779. https://doi.org/10.5194/gmd-12-4751-2019

Walker, A. P., Quaife, T., van Bodegom, P. M., De Kauwe, M. G., Keenan, T. F., Joiner, J., et al. (2017). The impact of alternative trait-scaling hypotheses for the maximum photosynthetic carboxylation rate (V-cmax) on global gross primary production. *New Phytologist*, *215*(4), 1370-1386. https://nph.onlinelibrary.wiley.com/doi/pdfdirect/10.1111/nph.14623?download=true

Wang, H., Jiang, F., Liu, Y., Yang, D., Wu, M., He, W., et al. (2022). Global Terrestrial Ecosystem Carbon Flux Inferred from TanSat XCO_2 Retrievals. *Journal of Remote Sensing, 2022,* 1-12. https://doi.org/10.34133/2022/9816536

Wang, H., Jiang, F., Wang, J., Ju, W., & Chen, J. M. (2019). Terrestrial ecosystem carbon flux estimated using GOSAT and OCO-2 XCO_2 retrievals. *Atmospheric Chemistry and Physics*, *19*(18), 12067-12082. https://doi.org/10.5194/acp-19-12067-2019

Wang, J., Jiang, F., Wang, H., Qiu, B., Wu, M., He, W., et al. (2021). Constraining global terrestrial gross primary productivity in a global carbon assimilation system with OCO-2 chlorophyll fluorescence data. *Agricultural and Forest Meteorology*, *304-305*. https://doi.org/10.1016/j.agrformet.2021.108424

Wunch, D., Wennberg, P. O., Toon, G. C., Connor, B. J., Fisher, B., Osterman, G. B., et al. (2011). A method for evaluating bias in global measurements of CO_2 total columns from space. *Atmospheric Chemistry and Physics*, *11*(23), 12317-12337. https://doi.org/10.5194/acp-11-12317-2011

Yue, X., & Unger, N. (2015). The Yale Interactive terrestrial Biosphere model version 1.0: description, evaluation and implementation into NASA GISS ModelE2. *Geoscientific Model Development*, *8*(8), 2399-2417. https://doi.org/10.5194/gmd-8-2399-2015

Zaehle, S., & Friend, A. D. (2010). Carbon and nitrogen cycle dynamics in the O-CN land surface model: 1. Model description, site-scale evaluation, and sensitivity to parameter estimates. *Global Biogeochemical Cycles*, *24*. https://doi.org/10.1029/2009gb003521

Zhang, H. F., Chen, B. Z., van der Laan-Luijk, I. T., Machida, T., Matsueda, H., Sawa, Y., et al. (2014). Estimating Asian terrestrial carbon fluxes from CONTRAIL aircraft and surface CO_2 observations for the period 2006–2010. *Atmospheric Chemistry and Physics*, *14*(11), 5807-5824. https://doi.org/10.5194/acp-14-5807-2014